JACS
JOURNAL OF THE AMERICAN CHEMICAL SOCIETY
ARTICLE
pubs.acs.org/JACS

Particle Size, Shape and Activity for Photocatalysis on Titania Anatase Nanoparticles in Aqueous Surroundings

Ye-Fei Li and Zhi-Pan Liu*

Shanghai Key Laboratory of Molecular Catalysis and Innovative Materials, Department of Chemistry, Key Laboratory of Computational Physical Science (Ministry of Education), Fudan University, Shanghai 200433, China

S Supporting Information

ABSTRACT: TiO_2 nanoparticles have been widely utilized in photocatalysis, but the atomic level understanding on their working mechanism falls much short of expectations. In particular, the correlation between the particle structure and the photocatalytic activity is not established yet, although it was observed that the activity is sensitive to the particle size and shape. This work, by investigating a series of TiO_2 anatase nanoparticles with different size and shape as the photocatalyst for water oxidation, correlates quantitatively the particle size and shape with the photocatalytic activity of the oxygen evolution reaction (OER). Extensive density functional theory (DFT) calculations combined with the periodic continuum solvation model have been utilized to compute the electronic structure of nanoparticles in aqueous solution and provide the reaction energetics for the key elementary reaction. We demonstrate that the equilibrium shape of nanoparticle is sensitive to its size from 1 to 30 nm, and the sharp crystals possess much higher activity than the flat crystals in OER, which in combination lead to the morphology dependence of photocatalytic activity. The conventionally regarded quantum size effect is excluded as the major cause. The physical origin for the shape−activity relationship is identified to be the unique spatial separation/localization of the frontier orbitals in the sharp nanoparticles, which benefits the adsorption of the key reaction intermediate (i.e., OH) in OER on the exposed five-coordinated Ti of {101} facet. The theoretical results here provide a firm basis for maximizing photocatalytic activity via nanostructure engineering and are also of significance for understanding photocatalysis on nanomaterials in general.

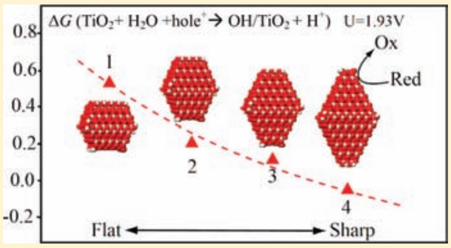

1. INTRODUCTION

It has been a consistent goal pursued by chemists to transform chemicals efficiently with solar energy. As one of the most important photocatalysts, TiO_2-based materials have demonstrated a great potential in many important redox reactions, including water splitting to generate O_2 and H_2.[1] In addition to the traditional measures by adding dopants to improve photocatalytic performance,[2−6] increasing evidence from recent studies show that the morphology of TiO_2 nanoparticle, not only the size but also the shape and the exposed facets, can be also important, which may affect the photocatalytic activity significantly.[7−12] This finding is intriguing in the sense that certain nanoparticle structure might be the key for achieving the high photocatalytic activity. To date, an atomic-level understanding on the prototypical TiO_2 nanoparticle system is urgently called for. New experimental or theoretical techniques are much desired to assess the quantum nature of nanosized particles and to treat properly the important issues in the photoreaction, such as the solid−liquid interface, the specific surface sites (e.g., terrace, steps), and the elementary chemical reactions.

Although the discovery of the photocatalytic water splitting on TiO_2 can be dated back to 1970s,[1] only recently it became possible to correlate the photocatalytic activity of TiO_2 nanoparticles with their morphology, thanks to the great advance in nanomaterial science. It was found in many photo-oxidation reactions that the sharp TiO_2 anatase nanocrystals (anatase is the most stable phase in TiO_2 nanoparticles) with a long distance in the [001] direction ($d_{[001]}$) has a high catalytic activity. For example, Murakami et al., showed that the activity of acetaldehyde decomposition is obviously higher in sharp nanocrystals dominated by {101} facet,[8] and the similar phenomenon was observed by Cho et al.[9] and Amano et al.[10] in chloroform and alcohol photodecomposition. By using a total scattering technique, Cernuto et al. investigated methylene blue decomposition on TiO_2 nanoparticles from 4 to 10 nm and found that the photo-oxidation efficiency is sensitive to both the size and the shape.[7] The microscopic origin behind is still subject to debate, and a number of possible causes have been proposed, focusing on different aspects of photoreaction, for example, the carrier mobility,[13] the conduction band position,[14] and the surface structure.[11,12]

The diverse views in literatures reflect the intrinsic complexity of the photocatalytic process, which comprises multiple elementary steps, such as the adsorption of reactants, the photoexcited electron−hole generation and separation, and the subsequent reduction and oxidation reactions. Apparently, without knowing the rate-determining step of the photocatalytic reaction, it is hard to pinpoint which observable of material is central to photoactivity. Nevertheless, among the views suggested, the surface structure sensitivity is perhaps most appealing, as proposed by Ohno et al., who first observed that the reductive deposition of

Received: July 2, 2011
Published: August 31, 2011

Pt^{2+} to Pt occurs preferentially on the {101} facet of TiO_2 anatase nanoparticle.[12] Apart from this photoreduction reaction, the photo-oxidation of typical molecules also appears to prefer the {101} facet of anatase nanoparticle.[10,13] The surface structure sensitivity in photocatalysis, more specifically, in photo-oxidation, is however not fully confirmed/understood yet. As a preliminary survey, we have studied the photocatalytic water oxidation on extended anatase surfaces in aqueous solution with density functional theory (DFT) calculations recently and found that the activity of OER is not sensitive to the surface structure of anatase.[15] The first proton removal in water oxidation, being the rate-determining step, exhibits the similar energy costs on three typical anatase surfaces. This was also confirmed by a recent experimental study using a single-molecule imaging method, which showed that the photo-oxidation reaction can occur on both {101} and (001) facets on large TiO_2 anatase particles (4 μm size).[16] It is thus implied that the observed morphology dependence of photo-oxidation activity might be unique to small nanoparticles, which behave quite differently from the surfaces of large particles.

In this work, we go further to explore the geometrical and the electronic properties of TiO_2 nanoparticles, aiming to identify the key factors dictating the photo-oxidation activity and understand why the morphology of nanoparticle matters. More than 10 different TiO_2 anatase nanoparticles ranging from 1.2 to 2.7 nm (diameters) are constructed and investigated in detail. Large-scale periodic DFT calculations integrated with the recently developed continuum solvation model based on a modified Poisson−Boltzmann equation[15,17−21] are performed to examine systematically the band structure, the carrier mobility, the surface energetics, and the OER activity of these nanoparticles in aqueous solution. From thermodynamics analysis, we show that the sharp anatase particles dominated by {101} facets could be inherently more active in photo-oxidation. The physical origin for the shape-controlled photocatalytic activity is revealed, and the puzzles on the surface structure sensitivity are clarified.

2. METHODOLOGY AND CALCULATION DETAILS

All DFT calculations were performed using the SIESTA[22,23] package with numerical atomic orbital basis sets[24] and Troullier−Martins norm-conserving pseudopotentials.[25] The exchange−correlation functional utilized was generalized gradient approximation Perdew, Burke, and Ernzerhof (GGA-PBE),[26] and the optimized double-ζ plus polarization (DZP) basis set was employed.[24,27] The semicore 3s and 3p states of Ti were included. The cutoff for the real space grid was set as 150 Ry. The L-Broyden−Fletcher−Goldfarb−Shanno (BFGS) method was employed for geometry relaxation until the maximal forces on each relaxed atom were less than 0.09 eV/Å and the difference of the total energy between two consecutive geometrical optimization steps is below 3 meV. Large unit cells (e.g., 75 × 50 × 50 Å) have been utilized to incorporate nanoparticles with the vacuum spacing being at least 25 Å. The periodic slab models were used to calculate the extended (101) and (001) surfaces, and the calculation details were described previously.[15] The solid−liquid interface between the nanoparticle and the aqueous solution was modeled by using the periodic continuum solvation model based on modified Poisson−Boltzmann equation (CM-MPB), which accounts for the long-range electrostatic interaction due to solvation.[15,17−21] Within the CM-MPB framework, it is convenient to align the band position of different nanoparticles and extended surfaces with the same solution level (e.g., ~25 Å away from the surface).

The method for computing the ΔG of the photo-oxidation reaction involving holes has been described in our previous work[15] and is thus only briefly mentioned here. In this work, we focused on the first proton removal step in OER on anatase particles, e.g., $(TiO_2)_s + H_2O + \text{hole}^+ \rightarrow (TiO_2)_s{-}OH^* + H^+$ (* denotes the adsorption state) on {101} facet, since this is the rate-determining step.[15] By using the standard hydrogen electrode (SHE) as the reference, $H^+ + e^- \rightarrow 1/2H_2$ (pH = 0, p = 1 bar, T = 298.15 K), we derive the Gibbs free energy change (ΔG_{OER}) of this first proton removal step as

$$\begin{aligned}\Delta G_{OER} = {} & G[(TiO_2)_s - OH] \\ & + 1/2G[H_2] - G[H_2O] - G[(TiO_2)_s] - |e|U\end{aligned} \qquad (1)$$

where U is the equivalent electrochemical potential of a hole with respect to SHE (~4.6 V in experiment[28]). To compare with the results on the extended surfaces[15] conveniently, we also set U = 1.93 V vs SHE in this work, i.e., 0.7 V overpotential with respect to the standard equilibrium potential of OER (1.23 V vs SHE). It should be mentioned that for aqueous H_2O and gaseous H_2, the large entropy term is essential to be included in computing ΔG_{OER} in eq 1, and the standard thermodynamic data[29] was utilized to obtain the entropy contributions. By further incorporating zero-point energies and enthalpy contribution from 0 to 298 K of free molecules,[30] $G[H_2O]$ and $G[H_2]$ are determined to be 0.57 and 0.31 eV lower compared to the total energy of the corresponding free molecules (E at 0 K), respectively.

There are two important issues that are worthwhile of special attention regarding the first proton removal step of OER. First, the proton removal is a redox reaction, which involves the hole transfer and proton removal with the surface being oxidized at the final state. This is different from H_2O dissociation on surface ($H_2O \rightarrow OH^* + H^*$), where both H and OH adsorb on the surface, and the surface is not reduced/oxidized at the final state. In fact, different anatase facets can have distinct activity for H_2O dissociation. For example, H_2O will dissociate facilely on clean (001) surface in aqueous solution and reach to a 0.5 ML, while on the (101) surface, H_2O dissociation is kinetically hindered.[15] For OER, it is the proton removal step (an oxidation reaction) that matters. At the final state, the stoichiometric surface is oxidized by the newly formed OH (on (101)) or terminal O (on (001)), which contributes critically to the energy cost of the reaction.[15] The distinction on the redox behavior between H_2O dissociation and the proton removal explains why the measured energy cost for the first proton removal step on (101), (001), and (102) surfaces are rather similar,[15] but the activity for dissociating H_2O differs greatly on the surfaces.

Second, eq 1 measures the thermodynamics of the first proton removal step of OER, the value of which can be calculated quantitatively from current DFT methods with the contribution of electron/hole pairs being folded into a correction term, $|e|U$. Microscopically, it remains unclear how this oxidation step occurs kinetically; specifically, how the hole transfer from substrate to water molecule (an excited state) and the bond breaking involving the proton removal are coupled in real time, which is however beyond the ground-state DFT framework, and further studies along this line are required. Obviously, an advantage of the thermodynamics analysis, as presented here and previously,[15] allows us to have a general overview of the OER potential energy

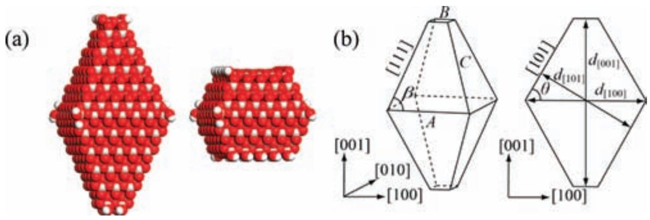

Figure 1. Anatase decahedral nanoparticles modeled: (a) illustration of the sharp (left) and the flat (right) particles; (b) the geometrical parameters utilized in Wulff construction: *A*, *B*, *C*, $d_{[101]}$, $d_{[001]}$ $d_{[100]}$, θ, and β represent the important lengths and angels, as indicated in (b). In the bulk truncated structure, θ is 68.4°, β is 69.8°, $C = (A - B)/(2\cos\beta)$, and $A = d_{[100]}$. Ti is gray, O is red, and H is white.

surface by focusing on the initial and final states before and after the charge transfer and therefore to identify the key elementary steps that possess the highest energy cost in the photoreaction. With the common knowledge in chemistry that thermodynamics are closely linked with kinetics for the same reaction under similar reaction conditions, we utilize ΔG_{OER} in eq 1 to probe the activity difference of the similar sites in different nanoparticles. As will be shown in Section 3.3, this value is indeed a sensitive measure, owing to the highly endothermic nature of the first proton removal of OER.

Model of Anatase Nanoparticles. It was observed in experiment that anatase nanoparticles possess approximate decahedral shape as controlled by the Wulff construction rule,[9,31] exposing mainly {101} and (001) facets, the two lowest surface energy surfaces. In line with this, we have constructed more than 10 differently shaped decahedral anatase nanoparticles, as shown in Figure 1 (the Cartesian atomic coordinate of such a typical nanoparticle is listed in Supporting Formation). From the Figure 1b, it can be seen that the size of particle is determined by the lengths along three directions, namely $d_{[101]}$, $d_{[100]}$, and $d_{[001]}$ or the edge lengths *A*, *B*, and *C*. It is often convenient to utilize a single parameter, the average diameter *D* ($D = (6V/\pi)^{1/3}$, the diameter of the corresponding sphere with the same volume *V*) to represent the size. The shape of particle is controlled by the ratio $d_{[001]}/d_{[101]}$, annotated as *S*. Obviously, the nanoparticles can be roughly categorized into two types, the sharp (large *S*) and the flat (small *S*) crystals, according to the value of *S* (see Figure 1a). In this work, we name all TiO_2 nanoparticles by $(TiO_2)_n$, *S*, where *n* is the number of TiO_2 unit and *S* is $d_{[001]}/d_{[101]}$.

It should be mentioned that the bulk-truncated nanoparticles with unsaturated edge/corner sites are highly unstable owing to the exposure of four-coordinated Ti (Ti_{4c}) or single-coordinated O (O_{1c}). To obtain a stable crystal, we have tested a few configurations by terminating the edge/corner Ti cations and O anions by additional OH groups and H atoms (from H_2O dissociation) while maintaining the correct chemical stoichiometry. The most stable configuration is selected after the structural optimization of the testing configurations. The termination of the edge/corner sites by H_2O is reasonable because too reactive Ti_{4c} or O_{1c} sites at the edge/corners will not be present[32] under hydrothermal synthetic conditions (H_2O dissociation on these sites are highly exothermic). Following this procedure, in all the nanoparticles modeled, all Ti sites are at least five-coordinated (Ti_{5c}), and the formal valence state of Ti, O, and H are +4, −2, and +1. The nanoparticles are further verified by finite-temperature first-principles molecular dynamics (FPMD) simulation to confirm the optimized structure is indeed stable (the calculated band structure and other properties shown below also demonstrate the validity of the model, where the experimental data are available for comparison). For example, for $(TiO_2)_{78}$, 1.82, no obvious structural reconstruction was observed in the FPMD simulation period (~1 ps) at 300 K with a Nose thermostat.

Table 1. Geometrical and Electronic Structure of Calculated Nanoparticles in Aqueous Solution (via Continuum Solvation)[a]

name	*D* (nm)	*S*	$d_{[100]}$ (nm)	$\varepsilon_{\mathrm{HOMO}}$/LUMO[b] (eV)	ΔE_g[c] (eV)	μ (m_e)[d]
$(TiO_2)_{58}$	1.20	0.90	1.14	−7.17/ −4.53	0.55	1.53
$(TiO_2)_{78}$	1.32	1.82	1.14	−6.94/ −4.35	0.51	1.35
$(TiO_2)_{97}$	1.48	0.68	1.53	−7.15/ −4.65	0.41	1.29
$(TiO_2)_{139}$	1.70	1.36	1.53	−7.08/ −4.59	0.40	1.02
$(TiO_2)_{159}$	1.78	2.04	1.53	−6.95/ −4.49	0.38	1.00
$(TiO_2)_{218}$	2.06	1.09	1.91	−7.09/ −4.67	0.34	0.83
$(TiO_2)_{260}$	2.18	1.63	1.91	−7.02/ −4.68	0.25	0.96
$(TiO_2)_{280}$	2.22	2.17	1.91	−6.96/ −4.58	0.30	0.82
$(TiO_2)_{315}$	2.28	0.90	2.29	−7.15/ −4.75	0.32	0.74
$(TiO_2)_{387}$	2.56	1.36	2.29	−7.06/ −4.76	0.22	0.80
$(TiO_2)_{429}$	2.64	1.82	2.29	−6.99/ −4.73	0.18	0.87
$(TiO_2)_{449}$	2.68	2.25	2.29	−6.96/ −4.67	0.21	0.76
(101)	–	–	–	−6.93/ −4.72	0.12	–
(001)	–	–	–	−6.90/ −4.71	0.10	–

[a] For comparison, the band structure data for extended surfaces, (101) and (001) are also shown. [b] $\varepsilon_{\mathrm{HOMO/LUMO}}$ is the energy position of HOMO/LUMO with respect to the solution level. [c] ΔE_g is the calculated band gap change with respect to the anatase bulk. [d] The effective mass of carrier.

3. RESULTS

3.1. Electronic Structure for Anatase Nanoparticles in Aqueous Solution.

To probe the quantum size effect, it is essential to gather an overview on the electronic structure of nanoparticles in aqueous solution and compare them with those from extended surfaces, such as (101) and (001). In this work, we have investigated 12 different Wulff nanoparticles, ranging from 204 atoms (containing 58 TiO_2 unit) to 1371 atoms (containing 449 TiO_2 unit) with different size (*D*) and shape (*S*). The calculated results are summarized in Table 1, including the energy position of the highest occupied molecular orbital (HOMO) and

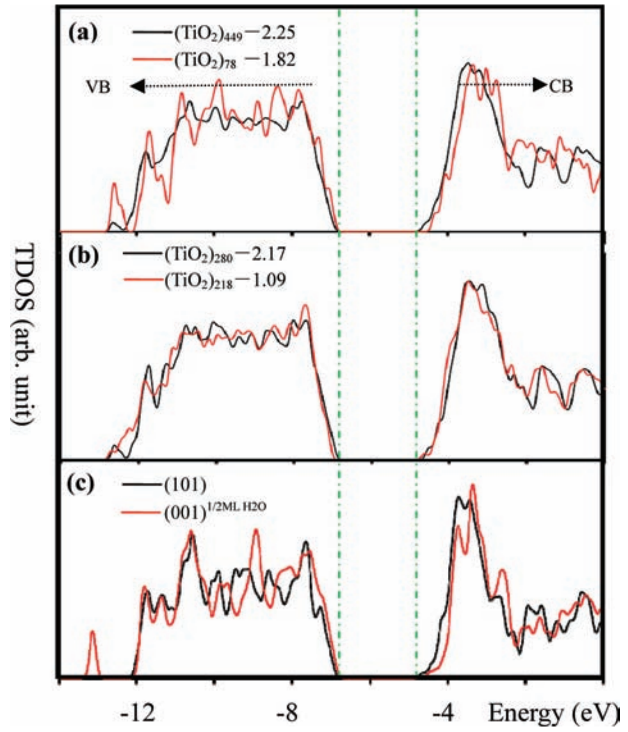

Figure 2. TDOSs of four selected anatase nanoparticles, extended (101) and (001) surfaces. The green dotted lines indicate the top edge of the valence band (VB) and the bottom edge of the conduction band (CB) of (101) surface.

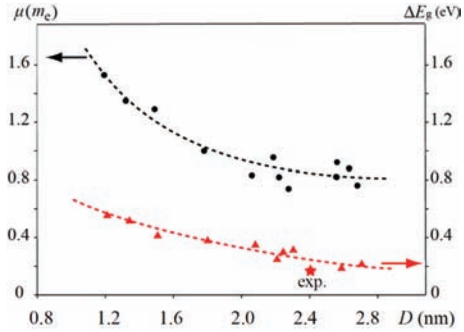

Figure 3. Calculated band gap change (ΔE_g) and the effective mass of carrier (μ) of anatase nanoparticles. The experimental value is taken from ref 34.

the lowest unoccupied molecular orbital (LUMO) ($\varepsilon_{\mathrm{HOMO/LUMO}}$) and the band gap change (ΔE_g) with respect to the anatase bulk. We found that, in general, compared to those of the extended surfaces, the energy position of HOMO at the top of valence band (-6.94 to -7.17 vs -6.93 eV) are generally lower, while that of LUMO at the bottom of the conduction band (-4.34 to -4.76 vs -4.72 eV) are similar or higher (i.e., in very small particles). As a result, the band gaps of the nanoparticles are always larger than the extended surface and the bulk. Furthermore, it is also obvious that with the increase of the particle size D, ΔE_g becomes smaller, inconsistent with the general knowledge on the quantum size effect that the larger the particle size is, the narrower the band gap of semiconductors will be. Importantly, we reveal that for nanoparticles larger than 2 nm, both the band gap and the $\varepsilon_{\mathrm{HOMO/LUMO}}$ converge rapidly toward those of the extended (101) and (001) surfaces (note that (001) surface in aqueous solution is already covered by half monolayer (ML) dissociated H_2O).[15,33] This implies that the quantum size effect may only be significant in very small TiO_2 anatase particles, e.g. <2 nm.

We then did a close inspection on the data in Table 1 in order to identify the individual effect of the size and the shape on the band structure. By focusing on particles with a similar shape but different sizes, e.g., the sharp crystals with S being ~2, including $(TiO_2)_{78}$, 1.82; $(TiO_2)_{159}$, 2.04; $(TiO_2)_{280}$, 2.17; and $(TiO_2)_{449}$, 2.25, and the flat crystals with S being ~1.2, including $(TiO_2)_{139}$, 1.36; $(TiO_2)_{218}$, 1.09; $(TiO_2)_{387}$, 1.36, we found that $\varepsilon_{\mathrm{HOMO}}$ in the same group are very similar, but $\varepsilon_{\mathrm{LUMO}}$ shifts down in energy with the increase of the particle size. This is illustrated in Figure 2a, where the total density of states (TDOSs) of two nanoparticles $(TiO_2)_{78}$, 1.82, and $(TiO_2)_{449}$, 2.25, in aqueous surroundings are plotted, and it shows that the $\varepsilon_{\mathrm{LUMO}}$ of the smaller $(TiO_2)_{78}$, 1.82, particle is obviously higher. On the other hand, for TiO_2 clusters with the similar size but different shapes, the change in the band structure is much less obvious. As illustrated in Figure 2b, for TDOS of $(TiO_2)_{218}$, 1.09, and $(TiO_2)_{280}$, 2.17, with D being around 2 nm, the TDOSs near the HOMO and LUMO regions of the two particles overlap closely with each other. From the figure, it is also clear that for the crystals larger than 2 nm, i.e., $(TiO_2)_{449}$, 2.25, $(TiO_2)_{218}$, 1.09, and $(TiO_2)_{280}$, 2.17), $\varepsilon_{\mathrm{HOMO}}$ and $\varepsilon_{\mathrm{LUMO}}$ are already very close to that of the extended surfaces (in Figure 2c). It might be mentioned that our calculated ΔE_g agree generally with those measured from experiment. For example, Kormann et al. found a blue shift of band gap by 0.15 eV for particles of ~2.4 nm[34] (note that it is a mean diameter from experiment); Anpo el al. reported a 0.16 eV gap change for anatase particles of ~3.8 nm[35] This indicates that the current model can correctly describe the physics of anatase nanoparticles.

Using the data of ΔE_g in Table 1, we can also calculate the effective mass of carrier for the anatase nanoparticles, which is the key parameter for measuring the carrier mobility in the photocatalytic process. The effective mass of carrier μ is defined by $\mu^{-1} = m_e^{*-1} + m_h^{*-1}$, being the reduced effective mass of the photoexcited electron m_e^* and the hole m_h^*. According to the Brus equation[36] (eq 2 below), μ can be calculated

$$\Delta E_g \approx \frac{2\hbar^2\pi^2}{D^2}\frac{1}{\mu} - \frac{3.6e^2}{\varepsilon D} \qquad (2)$$

where ε is the dielectric constant of the semiconductor; for anatase, it is ~31.[37] In Figure 3, we also plotted the calculated μ against the particle size. From the figure, we can see that μ generally decreases as the particle size D increases, in the same trend of ΔE_g versus D. This indicates that the larger TiO_2 particle would possess the higher carrier mobility. It is also noted that the μ converges rapidly to ~0.8 m_e for nanoparticles above 2 nm, which implies again that the quantum size effect is only obvious for very small TiO_2 nanoparticles, e.g., $D < 2$ nm. This is in fact a result of the rapid convergence of ΔE_g in anatase nanoparticles: ΔE_g is already below 0.2 eV for particles above 2 nm, the magnitude of which is much smaller than the band gap of bulk anatase (2.08 eV from DFT, 3.2 eV from experiment).[38] Considering that the experimentally synthesized anatase particles in photocatalysis are generally above 2 nm, we therefore expect that neither the carrier mobility nor the band gap could be the key factors for determining the photocatalytic efficiency. Experimentally, Cho et al. have shown that TiO_2 nanoparticles (3−33 nm) in aqueous solution possess the similar UV light adsorption and transmission spectra,[9] indicating the similar band structure for the synthesized TiO_2 nanoparticles.[35,39,40] They also suggested that the light transmission is not the cause for the difference in the photocatalytic activity.

3.2. Equilibrium Shape vs Size for Anatase Nanoparticles in Aqueous Solution. Based the Wulff construction rule, the equilibrium shape of crystal is related to its volume and thus is not independent of the particle size. From the DFT energetics of the nanoparticles, it is possible to deduce the equilibrium shape of anatase nanoparticles in aqueous surroundings by minimizing the total free energy of the particle under the constraint of the fixed volume. For large particles where the Wulff construction rule can be applied correctly, the shape is controlled by the surface energy, expressed as eq 3.[41] Given the particle in a decahedron shape as depicted in Figure 1b, we can use eq 4 to compute the $d_{[001]}$: $d_{[101]}$ ratio.

$$d_{[001]} : d_{[101]} = \gamma_{(001)} : \gamma_{\{101\}} \tag{3}$$

$$S = d_{[001]}/d_{[101]} = (1 - B/A)/\cos\theta \tag{4}$$

where A and B are the length of the bottom and the up bases of the side {101} trapezoid, respectively (see Figure 1b, note that A is also $d_{[100]}$). Using the periodic DFT/CM-MPB approach, we have computed the surface energy (γ) of {101} and (001) (with half ML dissociated water) in aqueous solution, which are 0.28 and 0.30 $J \cdot m^{-2}$, respectively. This yields an equilibrium S ($d_{[001]}$: $d_{[101]}$) being 1.07 in aqueous solution. It should be mentioned that this value is considerably smaller than that in vacuum, 1.73 from this work, 1.91 from previous first principle calculations by Lazzeri et al.,[42] and 1.4 estimated by classical Donnay−Harker rules.[43] Since the S of nanoparticles in vacuum is considerably larger, this implies that the shape of anatase nanoparticle should be very sensitive to the synthetic conditions in the crystal growth. Indeed, by controlling solvent pH and adding shape-controlling reagents (e.g., polyvinyl alcohol), the reported S value in experiment under hydrothermal conditions varies from 1 to 1.5.

It is of interest to compare our S value with those obtained from experiment. Penn et al. found that the S is close to 1 after 200 h hydrothermal crystallization in deionized water at pH ~ 5.5.[31] Ohno et al.[8] reported an average S being 1.25 ($d_{[101]}$ ~20 nm and $d_{[004]}$ ~25 nm according to X-ray diffraction) for anatase particles after 48 h hydrothermal preparation at pH ~ 7. Cho et al. revealed that the S can reach to 1.5 in deionized water at pH ~ 9.5.[9] Apparently, the predicted S value (1.07) in this work represents the thermodynamics limit for large anatase particles at the isoelectric point (for anatase this is at pH ~ 5.9)[44] in pure water without the addition of shape-controlling reagents. The theoretical value (1.07) should thus be compared to the experimental value of Penn et al.,[31] which is close to 1. From our results, it is also possible to explain the phenomenon that the S value of particles increases generally at elevated pH condition. We suggested that this could be caused by the hydroxyl anion adsorption on {101} facets where exposed Ti_{5c} are available. From our calculations, the free energy gain of the hydroxyl anion adsorption is 0.70 eV at pH ~ 7 and 1/6 ML coverage on (101) surface,[45] which can reduce the surface energy of {101} markedly. In contrast, the (001) surface in aqueous solution is already blocked by the half ML dissociated H_2O, and there is no free Ti sites exposed. As a result, the sharper nanocrystals will be synthesized at high pH conditions.

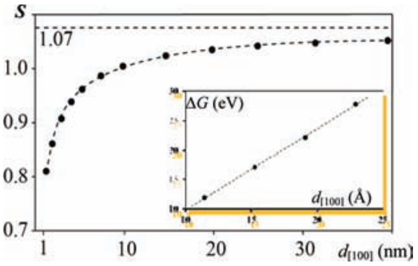

Figure 4. Correlation between the equilibrium shape (S) and the $d_{[100]}$ length of anatase nanoparticle. The insert shows the linear dependence ($R^2 = 0.9994$) of ΔG on $d_{[100]}$ at a fixed B length ($B = 3.82$ Å).

Equation 3 from the Wulff construction rule is in principle only valid for very large particles. The presence of the edges and corners in real nanoparticles is expected to affect the surface energy and in turn changes the equilibrium shape. To take into account of this effect and to predict more realistic S values for nanoparticles, we have carried out the following analysis based on the DFT energetics of the computed anatase particles. First, the ideal surface free energy (G^{i}_{sur}) of a decahedral particle is expressed as eq 5, which can be computed simply from the surface energy of extended surfaces $\gamma_{\{101\}}$ and $\gamma_{(001)}$ without considering the edge/corner effects. To obtain a realistic value G^{r}_{sur} for nanoparticles, a correction term ΔG (due to the presence of edge/corners) must be amended, as in eq 6.

$$G^{i}_{sur} = 2(A^2 - B^2)\tan\beta \cdot \gamma_{\{101\}} + 2B^2 \cdot \gamma_{(001)} \tag{5}$$

$$G^{r}_{sur} = G^{i}_{sur} + \Delta G \tag{6}$$

$$G^{r}_{sur} = G_{NP} - x \cdot G_{H2O} - n \cdot G_{bulk} \tag{7}$$

Next, from DFT energetics of the calculated nanoparticles in aqueous solution, we are able to calculate the G^{r}_{sur} using eq 7, where the $G_{NP/H2O/bulk}$ is the free energy of nanoparticle/H_2O/bulk anatase, and x and n account for the total number of the dissociated H_2O on the nanoparticle and the TiO_2 unit, respectively. By utilizing eqs 5−7, ΔG of six selected nanoparticles (i.e., $(TiO_2)_{449}$, 2.25; $(TiO_2)_{280}$, 2.17; $(TiO_2)_{260}$, 1.63; $(TiO_2)_{218}$, 1.09; $(TiO_2)_{159}$, 2.04; and $(TiO_2)_{78}$, 1.82) have been computed as listed in Table S1, Supporting Information. According to the shape of the decahedron nanoparticles, we can approximately attribute the origin of ΔG to a fixed number of edges and corners in the nanoparticle, which can be written as

$$\Delta G = 4A \cdot \gamma_A + 8B \cdot \gamma_B + 8C \cdot \gamma_C + \gamma_{cor} \tag{8}$$

where $A/B/C$ is the edge length as defined in Figure 1b, $\gamma_{A/B/C}$ is the free energy correction associated with the edge $A/B/C$, and γ_{cor} is the free energy correction due to the corners. The linear dependence of ΔG on the $A/B/C$ length has been observed in the calculated nanoparticles, as evidenced by the linear correlation between ΔG and A (also $d_{[100]}$) with the fixed B in the insert of Figure 4. By fitting the ΔG data in Table S1, Supporting Information with eq 8, we finally arrived at a formula, eq 9, to predict G^{r}_{sur}, where 1.3854, 0.8386, and 0.8520 are the fitted values (the unit for $A/B/C$ is Å and for G^{r}_{sur} is eV).

$$\begin{aligned} G^{r}_{sur} = {} & 0.0951 \cdot A^2 - 0.0576 \cdot B^2 \\ & + 1.3854 \cdot A - 0.8386 \cdot B - 0.8520 \end{aligned} \tag{9}$$

The creditability of this fitted formula is further checked by applying the formula to other nanoparticles that are not utilized in the fitting. We found that the predicted $G^{\mathrm{r}}_{\mathrm{sur}}$ from eq 9 agrees generally well with the DFT calculated one (within 2%). For example, for $(TiO_2)_{429}$, 1.82 (A = 22.896 and B = 7.632 Å) and $(TiO_2)_{387}$, 1.36 (A = 22.896 and B = 11.448 Å), the predicted surface energies from eq 9 are 70.97 and 63.57 eV, respectively, while those directly from DFT are 69.88 eV (1.5% error) and 63.41 eV (0.3% error), respectively.

Based on eq 9, we can finally predict the equilibrium shape S of nanoparticles by minimizing $G^{\mathrm{r}}_{\mathrm{sur}}$ at a given volume V ($V = 1/3 \cdot \tan\theta \cdot (A^3 - B^3)$) with the Lagrange multiplier method (details of derivation is provided in Supporting Information). In Figure 4, we have plotted the predicted S against the $d_{[100]}$. We can see that small nanoparticles exhibit much smaller value of S (i.e., being flatter), deviating from the Wulff limit 1.07 of large particles. With the increase of the particle size, the particle will be sharpened with a larger S. When the $d_{[100]}$ exceeds 30 nm (equivalent to D = 32.2 nm), the energy contribution of the edge and the corner diminishes, and the value of S approaches to the Wulff limit. Obviously, the equilibrium shape of nanoparticles changes dramatically below ∼30 nm, which spans in a much wider window compared to the variation of the band gap and the effective mass identified in Figure 3. The regime of the particle size from 1 to 30 nm is important in the sense that this is where the morphology-dependent photo-oxidation activity was observed in experiment,[7−9] which coincides interestingly with the rapid variation regime of the equilibrium shape in Figure 4. It is therefore important next to investigate whether the shape of the nanoparticle will influence the photoactivity.

The variation of the equilibrium shape against the nanoparticle size can lead to some intriguing phenomena. For example, the higher surface energy surface (001) will become preferentially exposed compared to the lower surface energy surface {101} in very small nanoparticles (i.e., $d_{[100]}$ below 10 nm, equivalent to D = 10.6 nm). This is apparently due to the influence of the edge/corner sites, which can be better stabilized in aqueous solution by dissociated H_2O molecules. Because the dissociation of H_2O at the edges/corners is highly exothermic, there is an intrinsic tendency to expose more edge/corners to allow for more H_2O dissociation. With a fixed volume, it is the flat, not the sharp, crystals that will have more edge/corner sites. On the other hand, the preference to adopt a flat shape is compromised by the additional energy cost to expose less stable (001) surface. For small nanoparticles, e.g., $d_{[100]}$ below 10 nm, the H_2O dissociation energy gain at the edge/corner sites is large enough to compensate the energy cost for exposing (001) facets, and thus the equilibrium shape is optimized toward the flat shape. For large particles, the H_2O dissociation energy gain is only a small term, and thus the equilibrium shape is dictated by Wulff principle.[41]

3.3. Photo-Oxidation Activity on Nanoparticles as Measured by OER Energetics.

In this work, we utilized OER in water oxidation as the model reaction to probe the morphology dependence of the photo-oxidation ability on anatase nanoparticles (also see Section 2 for special attentions of utilizing the current thermodynamics approach to compare activity). One of the advantages of this model system is that the rate-determining step of OER is already revealed by our previous work and the energetics on the extended anatase surfaces are available for direct comparison. In OER, the first proton removal step of water splitting, e.g. $H_2O + \mathrm{hole}^+ \rightarrow OH^* + H^+$, involves the highest energy cost and thus dictates the oxidation efficiency.[15] This key step involves the production of adsorbed OH species on the surface, which is also believed to be a major oxidant for the photo-oxidation reactions in aqueous solution in general.[46−48] From a practical point of view, OER is also one of the most challenging reactions in nature as it involves four electron transfers and 4.92 eV free energy cost at the standard condition. The intrinsic high barrier of OER can thus serve as a good basis for a quantitative analysis of the morphology-induced activity change. We have shown that even at an overpotential of 0.7 V (1.93 V vs SHE), the free energy cost (ΔG_{OER}) of the first proton removal reaction is 0.69, 0.61, and 0.63 eV on anatase (101), (001), and (112) surfaces, respectively. The high-energy cost of this step is attributed to the poor stability of the final state, e.g., the adsorbed OH on the Ti_{5c} site of (101), because the cationic Ti_{5c} is hard to be oxidized (i.e., Ti^{4+} to Ti^{5+} in the formal oxidation state). Naturally, one would ask whether the OH binding ability can be modified on nanoparticles and whether this depends on the morphology of the particle.

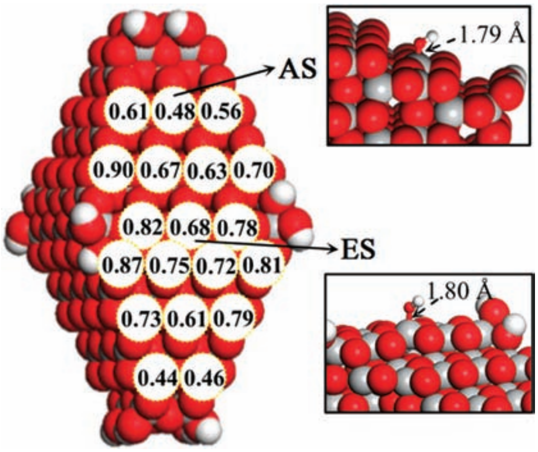

Figure 5. Calculated free energy change (ΔG_{OER}) of the first proton removal in OER on different Ti_{5c} sites of $(TiO_2)_{159}$, 2.04 at an overpotential of 0.7 V. The values of ΔG_{OER} are indicated at the corresponding Ti_{5c} sites. The OH adsorption structure at the AS at the sharp ends and the ES in the middle of the particle are also shown. Ti is gray, O is red, and H is white.

Different from the extended (periodic) surfaces, there are a large number of distinct surface Ti_{5c} sites on nanoparticles, even on the same microfacet, as shown in Figure 5. For a fast screening of the active site, we have first chosen a sharp nanoparticle $(TiO_2)_{159}$, 2.04 (D = 1.78 nm) as the model catalyst. The OH adsorption on all the possible Ti_{5c} sites has been computed to identify the most active site for the first proton removal step. The calculated ΔG_{OER} under an overpotential of 0.7 V (at the same condition as our previous work) is shown in Figure 5, which demonstrates that there is a large variation in ΔG_{OER} at different Ti_{5c} sites of the sharp nanoparticle. Because the initial state is the same, being the particle in aqueous solution, the large variation in ΔG_{OER} reflects the large difference in the OH adsorption energy at different Ti_{5c} sites. From Figure 5, two general features can be identified: (i) the axial sites (AS, labeled in Figure 5) at the sharp ends are the most active sites for OER, while the edge sites at the conjunction between {101} facets are typically the least active; and (ii) the terrace sites away from the edges are generally more active than the sites close to the edges.

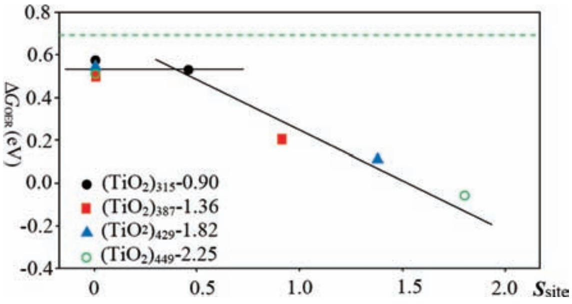

Figure 6. Calculated ΔG_{OER} at the AS and ES of four gradually sharpened nanoparticles. The green dotted line indicates the ΔG_{OER} value on the extended (101) surface (1/6 ML OH coverage).[15]

The difference of ΔG_{OER} between the AS and the equatorial site (ES, labeled in Figure 5) in the middle of the particle is of the most interest as it implies that the shape of particle could be critical to the activity. For convenience, we define a local S_{site} for a surface Ti_{5c} site as eq 10:

$$S_{site} = (1 - B'/A)/\cos\theta \qquad (10)$$

where B' is the length of the line inside the {101} trapezoid that passes the Ti_{5c} site and is in parallel with A and B (see Figure 1b). By this definition, S_{site} of AS is always larger than that of ES ($B' = A$, $S_{site} = 0$); S_{site} of the Ti_{5c} sites is always smaller than S of the particle (S_{site} of AS in large particles will be approximately equal to S of the particle).

To confirm the site sensitivity of ΔG_{OER}, we then studied the first proton removal reaction on a set of gradually sharpened nanoparticles (keeping the A length unchanged but varying the B length), i.e., $(TiO_2)_{449}$, 2.25; $(TiO_2)_{429}$, 1.82; $(TiO_2)_{387}$, 1.36; and $(TiO_2)_{315}$, 0.90. On each particle, we considered two sites, AS and ES. The calculated ΔG_{OER} of all the eight sites is plotted against the S_{site} of the sites in Figure 6 (note that $S_{site} = 0$ for all the ESs). We can see that ΔG_{OER} increases rapidly when S_{site} decreases from 1.81 to 0.45, and it remains relatively constant below 0.45. ΔG_{OER} for all the ESs is similar (~0.5 eV), which is 0.1−0.2 eV lower than those on extended surfaces, i.e., 0.61−0.69 eV.[15] Considering that the reported S of experimentally synthesized nanoparticles ranges from 1 to 1.5 (thus S_{site} must be larger than 0.45), the sensitivity of the photoactivity on the particle shape is thus expected for OER.

To understand why the adsorption energy of OH varies with S_{site}, we have first evaluated the Mulliken charges of the adsorbed OH at different adsorption sites and found that the OH group, no matter where it adsorbs, has the similar negative charges, ~ −0.3, indicating that the charge donation from the nanoparticle to the adsorbed OH is in fact not sensitive to the surface sites. It implies that the ionic bonding between OH and Ti_{5c} is not the major cause for the different OH binding strength at different sites. This is also confirmed by analyzing the solvation energy gain of the OH adsorption state with the CM-MPB method, which is a quantitative measure of the polarization strength of the adsorbed molecules. For strongly polarized molecules, the solvation energy will be much larger due to the additional electrostatic interaction caused by the solvation. In fact, we found that the solvation energy does not play important role in the site preference for the OH binding. For example, the OH adsorption energy at the AS is 0.35/0.37 eV larger than that that at the ES with/without the solvation in the $(TiO_2)_{429}$, 1.82. The ionic bonding via electrostatic interaction can thus be ruled out as the main cause for the site sensitivity of OH adsorption.

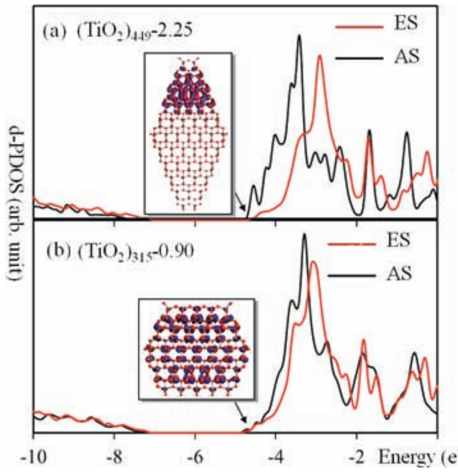

Figure 7. TDOS projected onto the 3d orbitals (d-PDOS) of Ti_{5c} at the AS and ES of $(TiO_2)_{449}$, 2.25 (a) and $(TiO_2)_{315}$, 0.90 (b). The 3D isosurface contour plots of the LUMOs are also shown, where the isosurface value is set as ±0.01 e/Å^3.

We therefore turn to examine the covalent bonding in the OH adsorption on nanoparticles. As shown previously for the OH binding on extended anatase (101) surface,[15] the dominant HO−Ti covalent bonding is through the O 2p orbital with the unoccupied Ti 3d states that locates at/near the LUMO. This picture of orbital mixing is also conserved for OH adsorption on nanoparticles (this can be clearly seen from the electron charge density difference contour plot for OH adsorption on nanoparticles, as shown Figure S1, Supporting Information). From the classic definition of the covalent bonding, both the energy position and the spatial distribution of the LUMO in the nanoparticles can be important for the binding strength. From Figure 2b, we already knew that the LUMO energy level is in fact not very sensitive to the particle shape, being generally at −4.7 eV. It is therefore expected that the spatial distribution of LUMO may be critical.

To this end, we have examined the frontier orbitals (HOMO and LUMO) of the four nanoparticles (see Figures S2 and S3, Supporting Information), focusing on their spatial distribution on the AS and the ES. In Figure 7, we plotted the TDOS projected onto the 3d orbitals of the Ti_{5c} at the AS and the ES in the $(TiO_2)_{449}$, 2.25 (Figure 7a), and $(TiO_2)_{315}$, 0.90 (Figure 7b). It shows that the difference in the d-PDOS between the two sites is very obvious in the sharp crystal $(TiO_2)_{449}$, 2.25. For example, the d-PDOS of the AS has a much larger intensity than that of the ES around the LUMO energies (~ −4.7 eV). We found that this is because the LUMO strongly localizes at the sharp ends, as shown in the insert of the figure. Since a larger extent of orbital overlap between O 2p orbital and the LUMOs can be achieved at the AS, it is not surprising that the OH strongly prefers to adsorb at the AS in the sharp crystal. In contrast, the LUMO of the flat crystal $(TiO_2)_{315}$, 0.90, is rather delocalized and the d-PDOSs of the two Ti_{5c} sites (AS and ES) overlap with each other around the LUMO energies. This is consistent with the fact that the OH adsorption energies are similar at the AS and the ES in the flat crystal (see Figure 6).

It should be mentioned that we also found that the HOMO of the nanoparticles always localizes in the equatorial region, away from the sharp ends (see Figure S2, Supporting Information). Consequently, the HOMO and LUMO are spatially separated in the sharp crystal, which is however not the case in the flat crystal. Because of the spatial separation, the sharper crystals are intrinsically more polarized and thus incur the larger solvation energy. For the four nanoparticles, $(TiO_2)_{449}$, 2.25; $(TiO_2)_{429}$, 1.82; $(TiO_2)_{387}$, 1.36; and $(TiO_2)_{315}$, 0.90, the calculated solvation energy gain of the particles are 0.236, 0.230, 0.224, and 0.222 J/m^2, the trend of which is in consistent with the trend of S on going from 2.25 to 0.9. It is indicated that the sharp crystals can be better stabilized in aqueous surroundings.

3.4. Discussion on the Morphology Dependence of Photoactivity. We are now at the position to address what is the physical origin of the morphology dependence of the photo-oxidation activity. We have first ruled out the possible causes related to the light adsorption ability and the carrier mobility as the band gap shift and the effective mass of carrier vary little for particles above 2 nm. Instead, we found that the shape of the nanoparticles varies rapidly for particles from 1 to 30 nm due to the large influence of the edges/corners in small particles that interact strongly with the water environment. By using OER as the probing reaction, we revealed that the free energy change of the rate-determining step is sensitive to the particle shape. From these theoretical results, we can conclude that the sharp nanoparticles possess the higher photoactivity for the following three reasons.

First, the HOMO−LUMO spatial separation is beneficial to the electron−hole pair separation at the early stage of photoexcitation process, which reduces the chance for the immediate electron−hole recombination. Second, the sharp crystals dominated by {101} facets can promote the photoreduction reaction. This will expedite the consumption of photoelectrons and thus reduce further the chance of electron−hole recombination. Fundamentally, this is because {101} facets are where the photoreduction occurs preferentially. We have shown that the (001) surface in aqueous solution is not active in photoreduction because the surface is already terminated by half ML dissociated water and the bottom edge of the conduction band locates mainly at the sublayers of the (001) surface.[15] This is also true in nanoparticles: The LUMOs locate generally on the surface of {101} facets (see Figure 7), independent of the shape of nanoparticle. Third, and most importantly, the sharp crystal can promote the photo-oxidation reaction by providing more active sites for the adsorption of key reaction intermediates. In OER, the OH production is the rate-determining step, and the OH adsorption energy can be systematically improved in the sharp nanoparticles, where more active Ti_{5c} sites with large S_{site} values are available.

This can be seen clearly in Figure 8, where the number of the axial Ti_{5c} sites (N_{site}) per unit volume for nanoparticles at their equilibrium shape (Figure 4) is counted with the S_{site} of these Ti_{5c} sites required to be larger than a preset critical value, i.e., 0.90, 0.95, and 1.00 (we choose these values by considering that $S \leq 1.07$ (see Figure 4) and S_{site} should be always smaller than S). Figure 8 shows that the curve of N_{site} per unit volume will exhibit a maximum where the optimum particle size can be identified. By lowering the critical value for S_{site}, i.e., from 1.00 to 0.90, the maximum peak shifts down toward the small particle size. For OER, as ΔG_{OER} is very sensitive to S_{site} (Figure 6), it is expected that the Ti_{5c} sites with the large S_{site} values, e.g., 0.95 and 1.00, dominate the catalytic activity, and thus the optimum particle size is predicted to be 15−20 nm. It can also be deduced that for reactions that are not sensitive to the S_{site} values, the optimum particle size should be well below 10 nm, simply because the smaller particles will have the larger surface area per unit volume. Obviously, the optimum particle size and thus the morphology for a photocatalytic reaction depend critically on the mechanism of the reaction and the reaction intermediates involved.

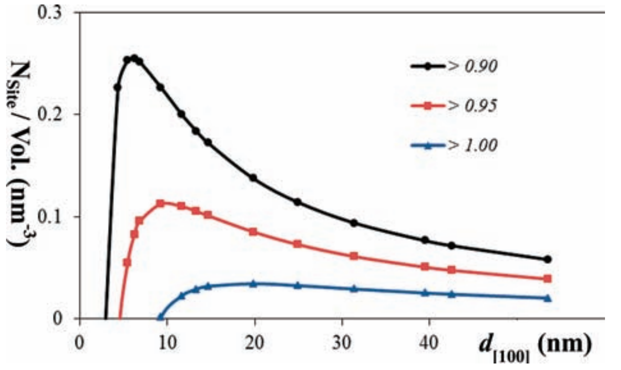

Figure 8. Number of the axial Ti_{5c} sites (N_{site}) per unit volume for anatase nanoparticles at the equilibrium shape (see Figure 4). N_{site} counts only the Ti_{5c} site, the S_{site} of which is above a preset value (i.e., 0.9, 0.95, and 1.0 in the figure).

It is interesting to notice that the photo-oxidation reaction prefers to occur at the ASs of the {101} facet, where the photoreduction reaction also takes place. Apparently, to avoid the immediate recombination of the electron−hole pair, it is critical that the reduction and oxidation reactions, involving photoelectrons and holes, respectively, occur at different temporal scales. In other words, the reduction needs to be much faster than the oxidation reaction. In fact, this can indeed be achieved in practice, for instance, by utilizing a facile reduction reaction (with a low overpotential). In OER of water oxidation, Fe^{3+} is often used as the sacrificing reagent, the reduction of which to Fe^{2+} is facile. By such means, the slower oxidation reaction decouples from the faster reduction reaction, and both reactions can occur at the same region. A recent experiment by Tachikawa et al. showed that the {101} facet can serve both as the oxidation and the reduction sites, demonstrating the importance of {101} facet in photocatalysis.[16] This is in line with the fact that {101} facets exposes Ti_{5c} sites, where the adsorption of molecules can take place.

Finally, we would like to highlight the key findings in this work that may be of significance for understanding photocatalysis on oxide nanoparticles in general. First, the photocatalytic reaction on oxide nanoparticles occurs not necessarily at the low-coordinated edge/corner sites. One important finding here is that very small oxide nanoparticles (e.g., below 5 nm) do not possess the highest photoactivity for OER. This is quite different from the conventional heterogeneous catalysis on metals, where the higher activity is often observed on small nanoparticles (e.g., below 5 nm) that contain a high concentration of low-coordinated surface defected sites (e.g., steps, kinks).[45] Clearly, the chemistry in metal nanoparticles is not simply transferable to oxide nanoparticles and vice versa. For anatase, the edge/corner sites in the bulk-truncated nanoparticles are too reactive and will be terminated by water readily in aqueous solution. It is the commonly available five-coordinated Ti cation sites at the terrace of {101} that are responsible for the photo-oxidation of water. Second, the size quantization effect may not be important in photocatalysis on oxide nanoparticles. For anatase, the band structure and the carrier mobility converge rapidly with the increase of particle size, and the size quantization effect is only obvious in very small nanoparticles (e.g., below 2 nm). It is anticipated that the free energy barrier of the elementary chemical reaction is still the key factor dictating the photoactivity on oxide nanoparticles, similar to that in conventional heat-driven catalysis.

4. CONCLUSIONS

This work represents a comprehensive survey of the electronic and geometrical properties and the photocatalytic activity of TiO_2 anatase nanoparticles in aqueous solution. More than 10 differently shaped TiO_2 anatase nanoparticles ranging from 1.2 to 2.7 nm are constructed and investigated by using periodic DFT calculations integrated with a modified Poisson−Boltzmann solver for modeling the solid−liquid interface. A quantitative correlation between the particle morphology and the photocatalytic activity is established and utilized to rationalize the experimental observations. Our main results are outlined as follows:

(i) The band gap shift and the carrier mobility of the nanoparticles converge rapidly with the increase of the particle size. A significant quantum size effect is observed only for very small nanoparticles, e.g., below 2 nm, which falls outside the particle size window identified in experiment for the morphology dependence of the photocatalytic activity.

(ii) By taking into account of the effects of edges and corners, the equilibrium shape of nanoparticle is correlated with the size quantitatively. It is found that with the decrease of particle size, the anatase nanoparticles become flatter owing to the stabilization of the edge/corner sites by the water environment.

(iii) Using OER in water photo-oxidation as the probing reaction, we evaluate the free energy of the first proton removal of water splitting, the rate-determining step, on different sites of nanoparticle. From thermodynamics analysis, we suggest that the sharp particles dominated by {101} facets could be inherently more reactive in photo-oxidation by exposing more active Ti_{5c} terrace sites. The physical origin is attributed to the unique HOMO−LUMO spatial separation in the sharp crystals that improves the covalent bonding between OH species and Ti_{5c} and simultaneously retards the electron−hole pair recombination.

(iv) To identify the optimum particle size for a photocatalytic reaction, we establish a quantitative correlation between the concentration of the axial Ti_{5c} sites near the sharp ends of nanoparticles and the particle size. For OER, the optimum particle size is predicted to be 15−20 nm, as its rate-determining step is highly sensitive to the position of the Ti_{5c} site.

■ ASSOCIATED CONTENT

Ⓢ **Supporting Information.** Details for the derivation of G^{r}_{sur} of nanoparticles; electronic charge density difference contour plot before and after the OH adsorption on ES and AS of $(TiO_2)_{449}$, 2.25; 3D isosurface contour plots of the frontier orbitals of $(TiO_2)_{449}$, 2.25; $(TiO_2)_{429}$, 1.82; $(TiO_2)_{387}$, 1.36; and $(TiO_2)_{315}$, 0.90. The Cartesian atomic coordinates of the optimized $(TiO_2)_{78}$, 1.82. This material is available free of charge via the Internet at http://pubs.acs.org.

■ AUTHOR INFORMATION

Corresponding Author

zpliu@fudan.edu.cn

■ ACKNOWLEDGMENT

This work is supported by National Nature Science Foundation of China (20825311), 973 program (2011CB808500), Science and Technology Commission of Shanghai Municipality (08DZ2270500), and Program for Professor of Special Appointment (Eastern Scholar) at Shanghai Institute of Higher Learning.

■ REFERENCES

(1) Fujishima, A.; Honda, K. *Nature* **1972**, *238*, 37.

(2) Kikkawa, H.; O'Regan, B.; Anderson, M. A. *J. Electroanal. Chem.* **1991**, *309*, 91.

(3) Asahi, R.; Morikawa, T.; Ohwaki, T.; Aoki, K.; Taga, Y. *Science* **2001**, *293*, 269.

(4) Ohno, T.; Mitsui, T.; Matsumura, M. *Chem. Lett.* **2003**, *32*, 364.

(5) Irie, H.; Watanabe, Y.; Hashimoto, K. *Chem. Lett.* **2003**, *32*, 772.

(6) Kato, H.; Kudo, A. *J. Phys. Chem. B* **2002**, *106*, 5029.

(7) Cernuto, G.; Masciocchi, N.; Cervellino, A.; Colonna, G. M.; Guagliardi, A. *J. Am. Chem. Soc.* **2011**, *133*, 3114.

(8) Murakami, N.; Kurihara, Y.; Tsubota, T.; Ohno, T. *J. Phys. Chem. C* **2009**, *113*, 3062.

(9) Cho, C. H.; Han, M. H.; Kim, D. H.; Kim, D. K. *Mater. Chem. Phys.* **2005**, *92*, 104.

(10) Amano, F.; Yasumoto, T.; Prieto-Mahaney, O.-O.; Uchida, S.; Shibayama, T.; Ohtani, B. *Chem. Commun.* **2009**, 2311.

(11) Ohno, T.; Sarukawa, K.; Matsumura, M. *J. Phys. Chem. B* **2001**, *105*, 2417.

(12) Ohno, T.; Sarukawa, K.; Matsumura, M. *New J. Chem.* **2002**, *26*, 1167.

(13) Wu, N.; Wang, J.; Tafen, D. N.; Wang, H.; Zheng, J.-G.; Lewis, J. P.; Liu, X.; Leonard, S. S.; Manivannan, A. *J. Am. Chem. Soc.* **2010**, *132*, 6679.

(14) Liu, G.; Sun, C.; Yang, H. G.; Smith, S. C.; Wang, L.; Lu, G. Q.; Cheng, H.-M. *Chem. Commun.* **2010**, *46*, 755.

(15) Li, Y.-F.; Liu, Z.-P.; Liu, L.; Gao, W. *J. Am. Chem. Soc.* **2010**, *132*, 13008.

(16) Tachikawa, T.; Yamashita, S.; Majima, T. *J. Am. Chem. Soc.* **2011**, *133*, 7197.

(17) Fattebert, J. L.; Gygi, F. *Phys. Rev. B* **2006**, *73*, 115124.

(18) Fattebert, J.-L.; Gygi, F. *J. Comput. Chem.* **2002**, *23*, 662.

(19) Fattebert, J.-L.; Gygi, F. *Int. J. Quantum Chem.* **2003**, *93*, 139.

(20) Wang, H.-F.; Liu, Z.-P. *J. Phys. Chem. C* **2009**, *113*, 17502.

(21) Fang, Y.-H.; Liu, Z.-P. *J. Am. Chem. Soc.* **2010**, *132*, 18214.

(22) Soler, J. M.; Artacho, E.; Gale, J. D.; García, A.; Junquera, J.; Ordejón, P.; Sánchez-Portal, D. *J. Phys.: Condens. Matter* **2002**, *14*, 2745.

(23) Sánchez-Portal, D.; Ordejón, P.; Artacho, E.; Soler, J. M. *Int. J. Quantum Chem.* **1997**, *65*, 453.

(24) Junquera, J.; Paz, O.; Sánchez-Portal, D.; Artacho, E. *Phys. Rev. B* **2001**, *64*, 235111.

(25) Troullier, N.; Martins, J.; Luriaas *Phys. Rev. B* **1991**, *43*, 1993.

(26) Perdew, J. P.; Burke, K.; Ernzerhof, M. *Phys. Rev. Lett.* **1996**, *77*, 3865.

(27) Anglada, E.; Soler, J. M.; Junquera, J.; Artacho, E. *Phys. Rev. B* **2002**, *66*, 205101.

(28) Bockris, J. O. M.; Khan, S. U. M. *Surface Electrochemistry*; Plenum. Press: New York, 1993, p 493.

(29) *CRC Handbook of Chemistry and Physics*. 84th ed.; Lide, D. R., Ed.; CRC Press: Boca Raton, FL, 2003−2004: 84th ed.;

(30) Liu, Z.-P.; Jenkins, S. J.; King, D. A. *J. Am. Chem. Soc.* **2004**, *126*, 10746.

(31) Penn, R. L.; Banfield, J. F. *Geochim. Cosmochim. Acta* **1999**, *63*, 1549.

(32) Gong, X.-Q.; Selloni, A.; Batzill, M.; Diebold, U. *Nat. Mater.* **2006**, *5*, 665.

(33) Gong, X.-Q.; Selloni, A. *J. Phys. Chem. B* **2005**, *109*, 19560.

(34) Kormann, C.; Bahnemann, D. W.; Hoffmann, M. R. *J. Phys. Chem.* **1988**, *92*, 5196.

(35) Anpo, M.; Shima, T.; Kodama, S.; Kubokawa, Y. *J. Phys. Chem.* **1987**, *91*, 4305.

(36) Brus, L. E. *J. Chem. Phys.* **1984**, *80*, 4403.

(37) Roberts, S. *Phys. Rev.* **1949**, *76*, 1215.

(38) Gratzel, M. *Nature* **2001**, *414*, 338.

(39) Wang, C.-C.; Zhang, Z.; Ying, J. Y. *Nanostruct. Mater.* **1997**, *9*, 583.

(40) Serpone, N.; Lawless, D.; Khairutdinov, R. *J. Phys. Chem.* **1995**, *99*, 16646.

(41) Wulff, G. *Z. Kristallogr. Mineral* **1901**, *34*, 449.

(42) Lazzeri, M.; Vittadini, A.; Selloni, A. *Phys. Rev. B* **2002**, *65*, 119901.

(43) Penn, R. L.; Banfield, J. F. *Am. Mineral.* **1998**, *83*, 1077.

(44) Kosmulski, M. *Adv. Colloid Interface Sci.* **2002**, *99*, 255.

(45) Shang, C.; Liu, Z.-P. *J. Am. Chem. Soc.* **2011**, *133*, 9938.

(46) Nosaka, Y.; Komori, S.; Yawata, K.; Hirakawa, T.; Nosaka, A. Y. *Phys. Chem. Chem. Phys.* **2003**, *5*, 4731.

(47) Murakami, Y.; Kenji, E.; Nosaka, A. Y.; Nosaka, Y. *J. Phys. Chem. B* **2006**, *110*, 16808.

(48) Hirakawa, T.; Yawata, K.; Nosaka, Y. *Appl. Catal., A* **2007**, *325*, 105.